electronics

MDPI

Article

High-Isolation MIMO Antenna for 5G Millimeter-Wave Communication Systems

Muhammad Bilal [1], Syeda Iffat Naqvi [1], Niamat Hussain [2], Yasar Amin [1] and Nam Kim [3,*]

[1] Department of Telecommunication Engineering, University of Engineering & Technology, Taxila 47080, Pakistan; muhammad.bilalvesper007@gmail.com (M.B.); iffat.naqvi@uettaxila.edu.pk (S.I.N.); yasar.amin@uettaxila.edu.pk (Y.A.)
[2] Department of Smart Device Engineering, Sejong University, Seoul 05006, Korea; hussain@chungbuk.ac.kr
[3] Department of Information and Communication Engineering, Chungbuk National University, Cheongju 28644, Korea
* Correspondence: namkim@chungbuk.ac.kr

Abstract: The work in this article presents the design and realization of a low-profile, four-port MIMO antenna supporting fifth-generation (5G) wireless applications operating at a millimeter-Wave (mm-Wave) band. Each MIMO antenna is a 2-element array fed with a corporate feeding network, whereas the single antenna is a patch with a bow-tie slot at the center and slits at the edges. The vertical and horizontal slots are incorporated as a Defected Ground Structure (DGS) to optimize the antenna performance. In addition, a slotted zig-zag decoupling structure is etched from edge to edge on the top side to enhance the isolation. Significant isolation (>−40 dB) is achieved between antenna elements by employing spatial and polarization diversity techniques. The proposed antenna covers the 5G mm-Wave band with a −10 dB bandwidth ranging from 27.6–28.6 GHz, whereas the maximum gain attained for the proposed structure is 12.02 dBi. Moreover, the lower correlation values, higher diversity gain, and lower channel capacity loss make it a suitable contender for 5G MIMO applications at the mm-Wave range.

Keywords: 5G antenna; antenna array; DGS; millimeter-wave antenna; MIMO; high isolation

Citation: Bilal, M.; Naqvi, S.I.; Hussain, N.; Amin, Y.; Kim, N. High-Isolation MIMO Antenna for 5G Millimeter-Wave Communication Systems. *Electronics* **2022**, *11*, 962. https://doi.org/10.3390/electronics11060962

Academic Editor: Dinh-Thuan Do

Received: 23 December 2021
Accepted: 7 March 2022
Published: 21 March 2022

1. Introduction

With the recent advancements in wireless communication technology, the fifth-generation (5G) new radio (NR) has drawn significant attention, and it is currently one of the most discussed technologies [1]. The limited available bandwidth in the microwave spectrum range, its low latency, and the incessantly growing demand for higher data rates have prompted the utilization of the mm-Wave spectrum (especially 24–100 GHz) for 5G applications [2,3]. The 5G systems are anticipated to administer seamless connectivity through prevailing technologies such as virtual reality, smart homes, telehealth, and Internet of Vehicles (IoV) [4]. Governments, the telecommunications industry, and regulatory bodies are working tirelessly to standardize and deploy 5G wireless communication systems. Global spectrum allocation demonstrates that most countries have considered 26 and 28 GHz bands for 5G communication [5,6].

Antenna design for the allocated 5G mm-Wave bands is rather challenging for antenna designers. As the atmospheric and propagation losses increase at the mm-Wave spectrum [7], high-gain antennas are therefore required for 5G communication. Various methodologies in practice meant to increase the gain of antennas have been reported in the literature, including superstate above patch antennas, stacking multiple patch substrates, lens coupled antennas, and Dielectric resonator antennas (DRAs) [8–13]. All these antennas have the advantage of having high gain. However, the drawbacks of high profiles, complex geometries, non-planar structures, and large sizes are also associated with these methodologies. Another widely used approach for the attainment of high gain is the antenna

array [14–16]. These studies show that the planar structure of the antenna arrays facilitates the ease of integration with electronic circuitry. However, although the signal strength increases due to high gain, antenna arrays have the same channel capacity as a single antenna due to their single feeding port. Lately, multiple-input-multiple-output (MIMO) technology has gained attention due to its promising features such as increased data rates and higher capacity, which are the requirements of 5G communication systems [17].

Recently, numerous mm-Wave antennas with high gain and/or MIMO have been reported in the literature [18–26]. The work in [18] presented a 4 × 4 Vivaldi antenna array. This antenna obtained a wide bandwidth, from 25 to 40 GHz, and a high gain of approximately 16 dBi. However, the design had large dimensions of 135 × 97 mm^2, and the array configuration was non-planar with a vertical stacking of substrate layers. The antenna design proposed in [19] was a patch antenna covering the 28 GHz mm-Wave band, where a split-ring metasurface was placed above the antenna to enhance the antenna performance. The antenna attained a peak gain of 11.94 dBi and a fractional bandwidth of 9.77 GHz after metasurface employment. However, although the proposed antenna had a high gain, it lacked the MIMO capability. In another work [20], the reported antenna was a two-port mm-Wave MIMO antenna. Due to the Electromagnetic Bandgap (EBG)-based reflector, the antenna showed improvement in gain and bandwidth, where the peak gain obtained was 11.5 dBi. However, the overall size of the proposed structure was large, in addition to the increased design and fabrication complexity. The work in [21] demonstrated a wideband, 9 × 9 element MIMO antenna operating at the mm-Wave band. The peak antenna gain was 7.8 dBi with a relatively large antenna size of 126 × 126 mm^2. Another 2-port MIMO antenna for mm-Wave communication was proposed in [22]. This antenna was simpler in design, although the peak gain obtained was 5.7 dBi for the operating band. In [23], a planar metamaterial-based 2-port MIMO antenna was proposed for the mm-Wave frequency band. The proposed antenna structure attained a maximum gain of 13.4 dBi, with an overall substrate size of 52 × 23 mm^2. The antenna design presented in [24] was a four-element mm-Wave MIMO antenna, with an overall size of 80 × 80 mm^2. The proposed antenna was wideband with a peak gain value of 11.45 dBi. However, although the proposed antenna attained wide bandwidth and high gain, the overall size of the antenna was comparatively large. Another mm-Wave MIMO antenna was demonstrated in [25]. This antenna was a 4-port MIMO structure where each element was a circular ring-shaped antenna. The maximum gain attained by the antenna was 6.1 dBi, whereas the substrate size was 30 × 30 mm^2. Similarly, the MIMO antenna presented in [26] was a 4-port structure with a board size of 30 × 35 mm^2. This antenna reported a wide bandwidth, whereas the peak gain attained was 8.3 dBi. It was observed that for all these antenna designs, if the antenna is able to attain high gain, either the design is complex with a large size, or it lacks the MIMO capability. On the other hand, if the antenna design is compact and simple, the high gain requirement for 5G communication at the mm-Wave spectrum is not achieved. Hence, a planar MIMO antenna with a compact size, higher isolation, and high gain is a real need of the time for the realization of 5G communication systems by employing the multi-path property.

Considering the above-mentioned challenges and discrepancies in the earlier reported works, a mm-Wave MIMO antenna with a high gain and a compact design is proposed in this article. The proposed antenna is a 4-port antenna with a simple structure and good MIMO performance. In order to obtain high gain, a two-element array with a corporate feed network and DGS is used. Additionally, a slotted structure is incorporated in between the antennas to lessen the mutual coupling. Moreover, the planar system enables the easy assimilation of the antenna with 5G devices. Therefore, the suitability of the presented antenna for 5G mm-Wave communication applications is ensured.

2. Antenna Design and Characterization

In this section, the design and characterization of the proposed antenna is discussed. The overall design process is shown in Figure 1. The design modeling starts with the

single-element antenna, followed by the two-element array, and finally, a MIMO structure is obtained for 5G mm-Wave applications. For modeling and optimization purposes, the EM simulator CST Microwave Studio is used, whereas the proposed antenna is etched on a Rogers RT/Duroid 5880 substrate with a thickness of h = 0.787 mm, ε_r = 2.2, and $tan\delta$ = 0.0009. The stepwise design process, optimization, and corresponding results are discussed in the succeeding sections, while the parametric values of the optimized proposed antenna are tabulated in Table 1.

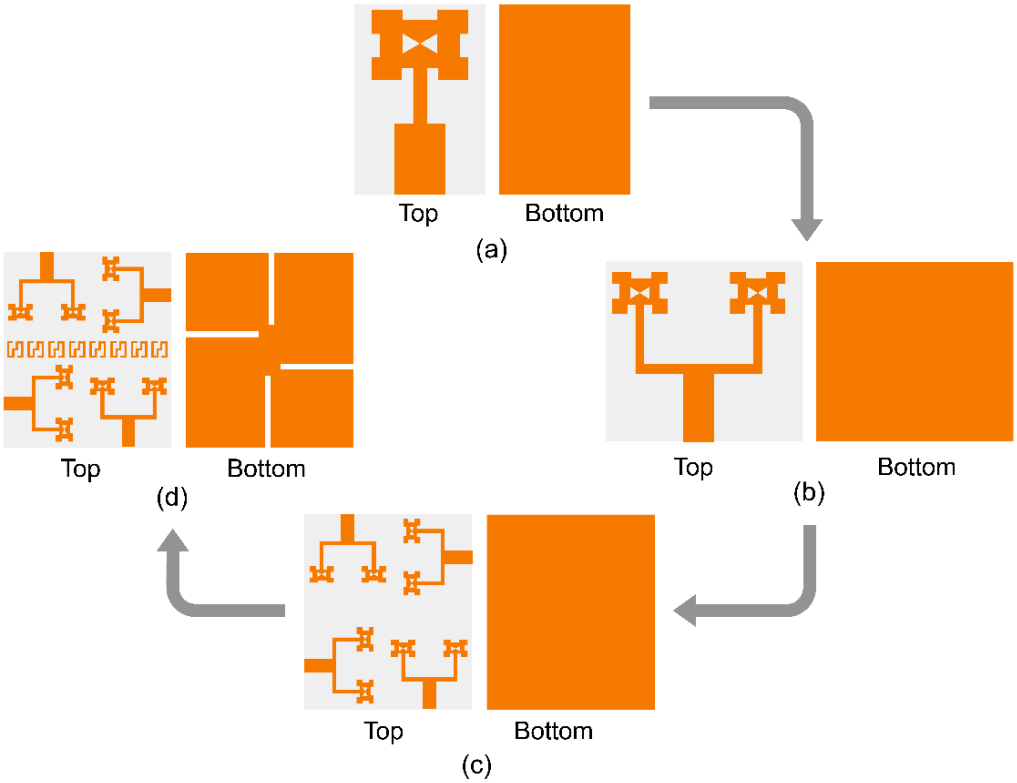

Figure 1. Overview of design process. (**a**) Single antenna; (**b**) Array structure; (**c**) MIMO configuration; (**d**) Decoupler and DGS incorporation.

Table 1. Optimized design parameters (all in millimeters).

Parameter	Value	Parameter	Value	Parameter	Value
W	6	L	8.5	G_1	0.5
W_{f1}	2.2	L_{f1}	3.1	G_2	1
W_{f2}	4.2	L_{f2}	2.4	L_{f3}	3.06
W_1	15.5	L_1	15.15	W_{f3}	8.7
L_{f4}	5.45	W_{f4}	5.45	H_1	0.787
W_3	30	L_3	35	D_x	2.91
D_y	3	L_x	13	L_y	1

2.1. Single Antenna

The design procedure starts with the single antenna. The geometrical configuration of the single-element antenna is illustrated in Figure 2a. The single antenna comprises of a rectangular patch with bow-tie-shaped slots at the center and rectangular slits at the top and sides of the patch. The overall substrate size of a single antenna is L × W. Firstly, a simple, inset-fed, rectangular-shaped patch antenna with a full ground layer is designed considering the well-established design equations [27]. The feedline is modified using a quarter-wave transformer-based matching network, as illustrated in Figure 2a. To ensure impedance matching, the Z-parameter is plotted in Figure 2b. To match the antenna to the

port, the 50 Ω impedance must be obtained. It is clear from Figure 2b that the real part of the impedance is nearly 50 Ω, whereas the imaginary part approaches zero at the resonant frequency. Hence, the port is well-matched.

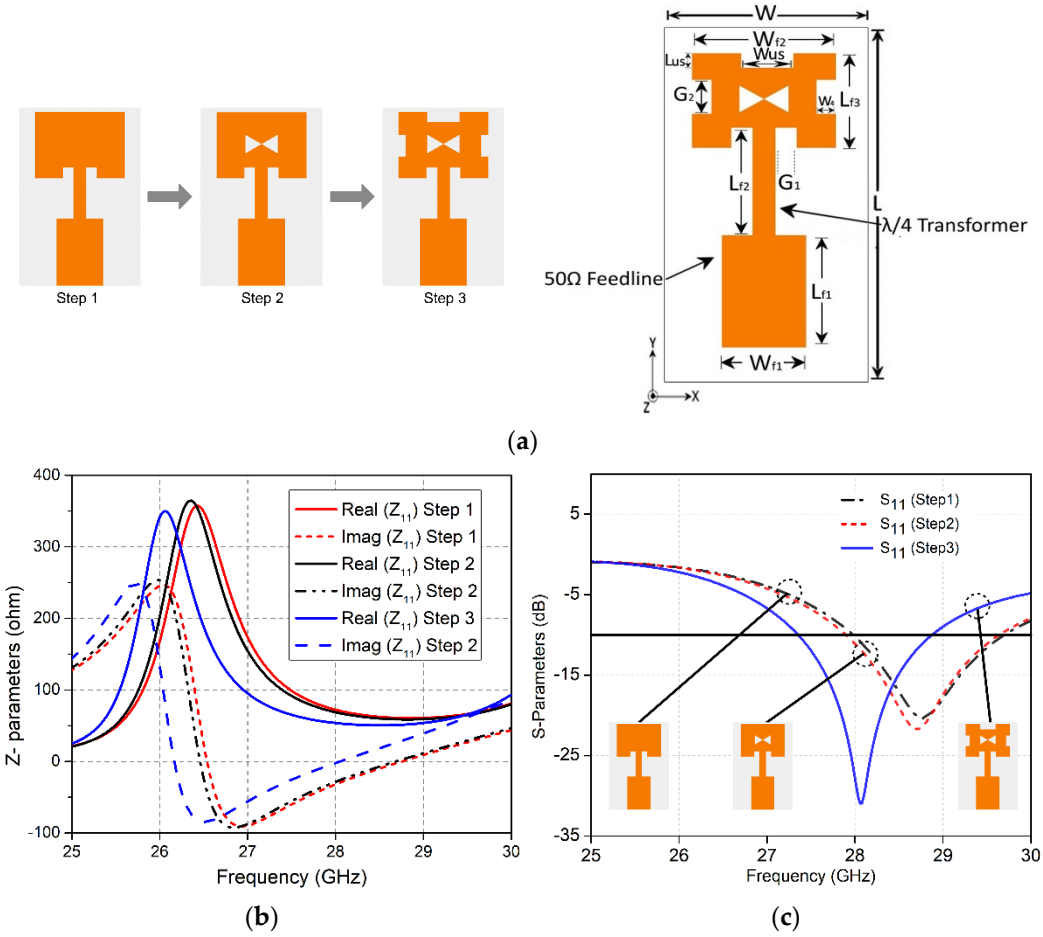

Figure 2. (**a**) The single antenna and its design procedure; (**b**) Z-parameter of the single antenna; (**c**) S-parameters of the single antenna.

In order to investigate the antenna performance, the S-parameters are analyzed. The S-parameter results for each optimization stage of the single antenna are exhibited in Figure 2c, which shows that this initial antenna resonates at the mm-Wave frequency band, ranging from 28–29.7 GHz. It is also evident through Figure 2b that the real part of the impedance is nearly 50 Ω at the central frequency of 28.8 GHz, whereas the imaginary part is around zero for the step 1 antenna. Later, a bow-tie-shaped slot is incorporated at the center of the patch. The frequency band shifts slightly. However, no significant change in impedance bandwidth is observed at this step. The antenna design is further modified by etching rectangular slits at the top and side edges of the patch, as illustrated in Figure 2a, so that the antenna resonates at the targeted central frequency, i.e., 28 GHz. The final optimized single antenna now resonates at 28 GHz, with a band ranging from 27.3 to 28.9 GHz, as shown in Figure 2c. The Z-parameter plot for the step 3 antenna in Figure 2b also depicts that the real part of the impedance is approximately 50 Ω at 28 GHz now, while the imaginary part is close to zero.

In order to investigate the operation mechanism of the antenna, surface current distribution at 28 GHz is provided in Figure 3 for all three design stages. It can be observed that current is mainly distributed around the feed line and at the edges of the patch antenna for the first step of the design process. Later, when the bow-tie-shaped slot is incorporated at the center of the patch antenna, a major current distribution is found near the bow-tie slot and at the edges of the antenna. The placement of the slot alters the current path, thus

increasing the path length. As a result, the frequency band is slightly shifted towards the lower frequency, as illustrated in Figure 2c. Finally, when slits are etched at the top and side edges of the antenna, current density is noted around the bow-tie slot and at the slits. The employment of the slits further increases the path length of the current, thus increasing the effective length of the antenna. This affects the resonant frequency, as evident from Figure 2c, where the resonant band has significantly shifted towards the lower frequency, thus attaining the desired resonant frequency. Therefore, the contribution of the bow-tie slot as well as slits at the top and side edges to attain the desired resonant band is exhibited through surface current density.

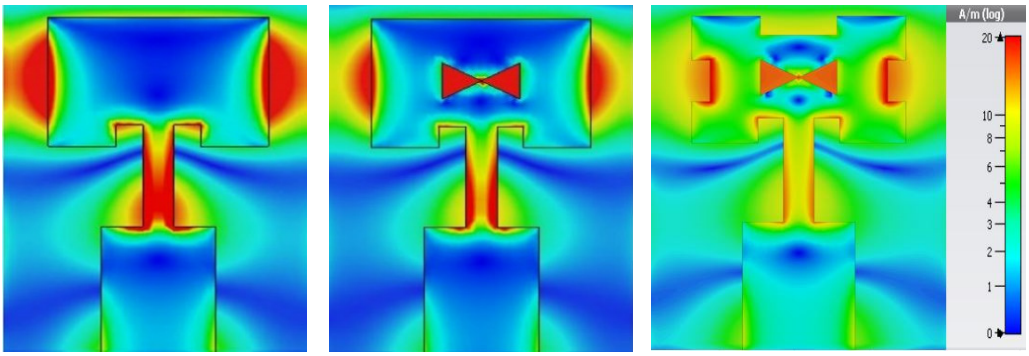

Figure 3. Surface current distribution at 28 GHz for each design stage of the single antenna.

Parametric Analysis

As it is evident from Figures 2c and 3, the rectangular slits at the top and side edges of the single-patch antenna play a vital role in shifting the resonance to the desired frequency band. Thus, this section provides a parametric analysis of important parameters. The length G_2 and width W_4 of the side slit plays a substantial role in designing the antenna in order to obtain the desired resonant frequency. If the length (G_2) of the side slit is set at 0.6 mm (0.056λ), the reflection coefficient curve in Figure 4a shows that that band is obtained at 28.5 GHz, within the range of 28–28.9 GHz. If G_2 is increased to 0.8 mm (0.074λ), a shift in the resonant band towards 28 GHz is observed. However, the resonant frequency is still not centered at 28 GHz. If G_2 is further increased and set to 1 mm (0.093λ), the resonant band shifts toward the desired frequency, and now the band is centered at 28 GHz. Hence, the optimized value for the length of the side slit is 1 mm (0.093λ), which demonstrates the improved antenna performance. The parametric analysis for the width W_4 of the side slit is illustrated in Figure 4b.

It is noticed that for the optimized value of W_4 = 0.45 mm, the band is centered at the targeted frequency with an operating band ranging from 27.7 to 28.5 GHz. Whereas for other values of W_4, the resonant band is shifted towards the higher frequency, not covering the desired band. Furthermore, poor impedance matching is observed for the values of W_4 = 0.15 mm and 0.30 mm. Therefore, the optimal value of W_4 is determined to be 0.45 mm, which corresponds to the electrical length of 0.042λ at the central frequency of 28 GHz.

Figure 4c,d exhibit the parametric analysis for the length L_{us} and width W_{us} of the slit at the top side of the patch antenna. It is demonstrated from the reflection coefficient results in Figure 4c that if the value of L_{us} is set at 0.15 mm and 0.30 mm, the desired resonant band is not covered. However, for the value of L_{us} = 0.45 mm (0.042λ), the resonant band covers the required mm-Wave band of 27.3–28.9 GHz, with the central frequency at 28 GHz. In addition to the attainment of the targeted frequency, a widening of the band is also observed for this value of L_{us}. Figure 4d illustrates that for the optimal value of W_{us} = 1.5 mm, the desired resonance is achieved, whereas for other values, i.e., 0.5 mm and 1.0 mm (which are equivalent to 0.014λ and 0.028λ, respectively), the resonance is shifted towards the lower frequency.

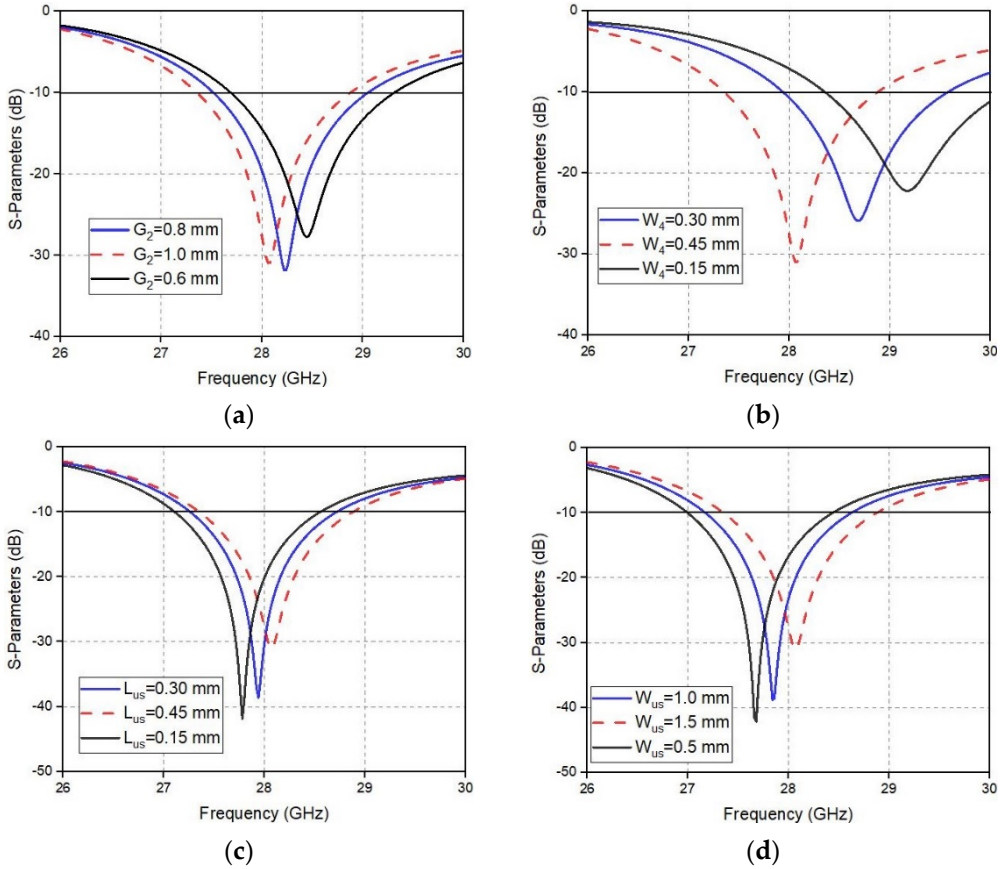

Figure 4. Parametric analysis of (**a**) Left slit length; (**b**) Left slit width; (**c**) Top slit length; (**d**) Top slit width.

2.2. Antenna Array

To obtain high gain, the single antenna is further progressed to a two-element array, where array elements are connected by a one-to-two corporate feed network, as illustrated in Figure 5a. For impedance matching, well-established characteristic equations [27] are used to calculate the line widths of the transmission network during the modeling process. Thus, the main feedline is matched at 50 Ω, while the branched network is at 100 Ω. The substrate dimensions of the array structure are L1 × W1 mm^2. This antenna array resonates at the band ranging from 27.4 to 28.5 GHz, as depicted in Figure 5c. It can be noticed that the obtained band for this modified structure is slightly narrow as compared to a single antenna, and that it also shifts upward; however, the bandwidth is still sufficient to enable 5G communication.

2.3. MIMO Structure

Later, the design is modified into a four-element MIMO configuration with an overall substrate size of $L_2 \times W_2$ mm^2, as depicted in Figure 5b. The analysis of simulated reflection coefficient results for MIMO antennas (Ant1–Ant4) demonstrates that all antennas exhibit almost similar behavior and obtained a resonant band at 27.4–28.5 GHz, also shown in Figure 5c. The transmission coefficient results plotted in Figure 5d show that the MIMO structure attained significant isolation between antenna elements, with the minimum obtained isolation being approximately −32 dB between Ant1 and Ant2 ($|S_{12}|$) for the entire resonant band.

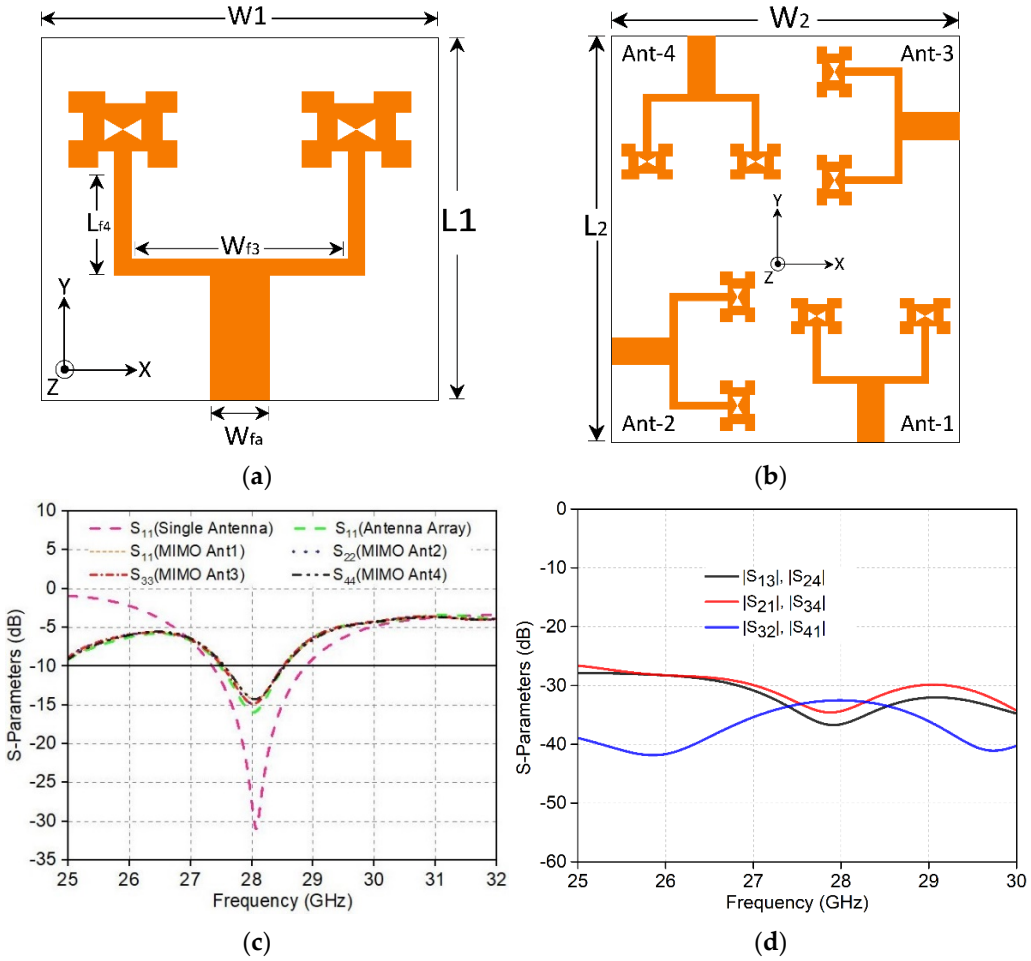

Figure 5. (**a**) Antenna array; (**b**) MIMO layout; (**c**) Reflection coefficient; (**d**) Transmission coefficient.

2.4. Performance Analysis of DGS and Decoupler

To enhance antenna radiation characteristics and to improve the isolation among MIMO antenna elements, a decoupling structure and a Defected Ground Structure (DGS) are introduced. The decoupler consists of a zig-zag pattern etched horizontally at the top layer, whereas the DGS is employed at the bottom layer comprising of four vertically and horizontally placed rectangular slots, as shown in Figure 6a. The incorporation of these structures results in the reduction of the near-field coupling effects between MIMO antennas, as exhibited by the transmission coefficient curves in Figure 6b. It can be noted that minimum isolation improves from −32 dB to −43 dB between Ant1 and Ant2 ($|S_{12}|$), whereas for other antenna elements, isolation is higher than this. Thus, an isolation increase of approximately 9 dB was achieved after the deployment of the decoupler and the DGS. Moreover, employing the decoupler and the DGS enhanced the antenna gain.

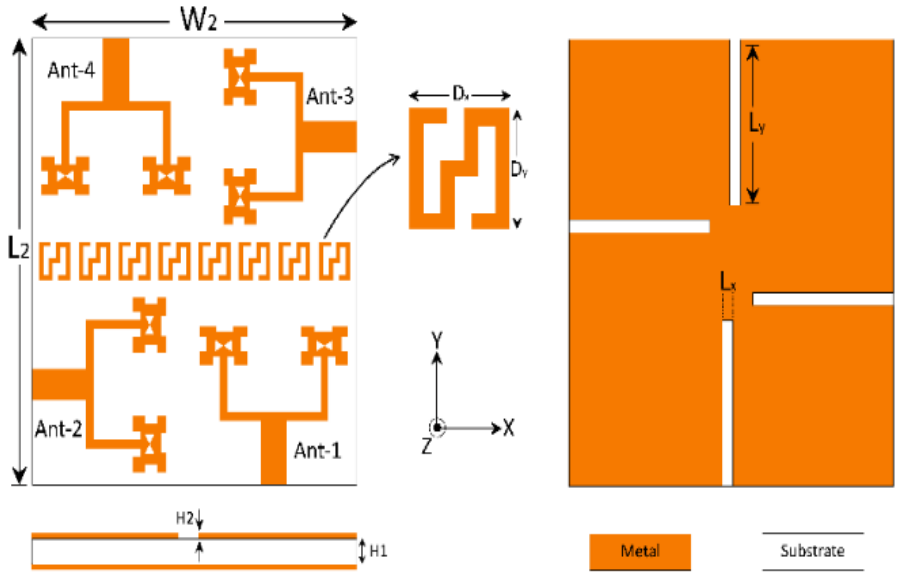

(**a**)

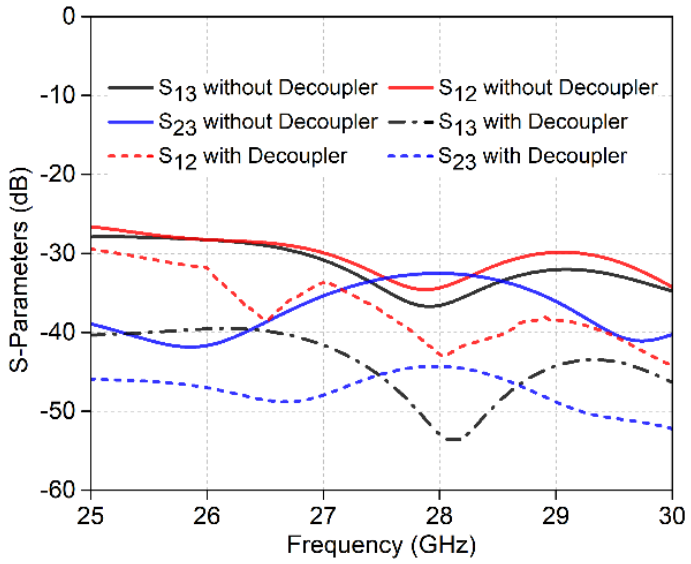

(**b**)

Figure 6. (**a**) Final proposed antenna with decoupler and DGS; (**b**) Transmission coefficient results with and without decoupler and DGS.

The contribution of these optimization techniques to enhance isolation by reducing mutual coupling between antenna elements is also validated through a surface current density at 28 GHz. Figure 7a illustrates that when Ant1 is excited before the involvement of the decoupler, and other antenna elements are terminated with a 50 Ω load, the coupled field is predominately observed on Ant3; on the other hand, a lower coupling current is distributed on Ant2 and Ant4. However, with a decoupling structure, the near-field coupling effects on neighboring radiators are minimized, as depicted in Figure 7b. Consequently, isolation among MIMO antenna elements is enhanced, as demonstrated earlier by the transmission coefficient curves in Figure 6b.

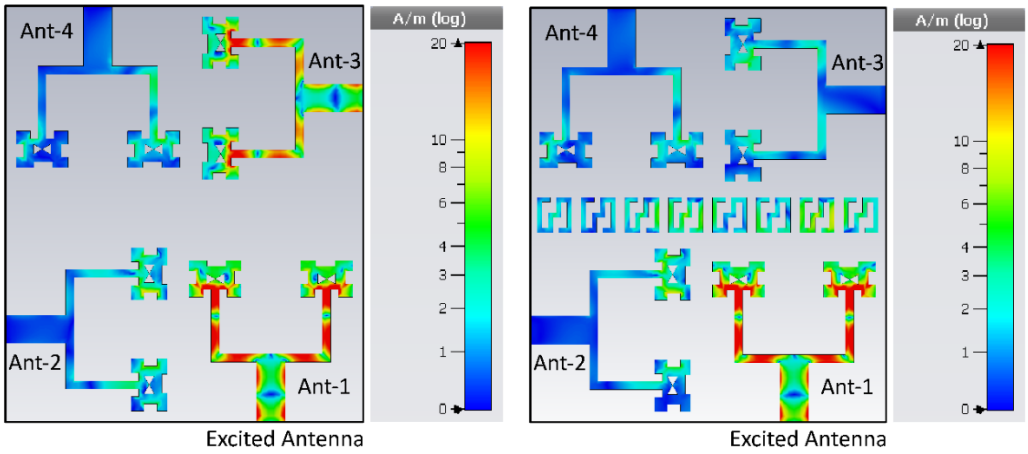

Figure 7. Surface current distribution at 28 GHz: (**a**) without decoupler; (**b**) with decoupler.

In order to describe the antenna performance at each design stage from the single element to the final proposed MIMO design, antenna gain is exhibited in Figure 8. It can be observed that the peak gain attained by the single antenna is 7.2 dBi. It can also be noted that the antenna gain for the array configuration exhibits significant improvement as compared to the single antenna with a peak gain of 11.3 dBi, as illustrated in Figure 8. The peak gain across the resonant band for MIMO antennas without the decoupler and the DGS nearly remains the same as the antenna gain for the array structure. However, peak gain improves to approximately 12.25 dBi for the resonating band when the decoupler and the DGS are incorporated, as shown in Figure 8.

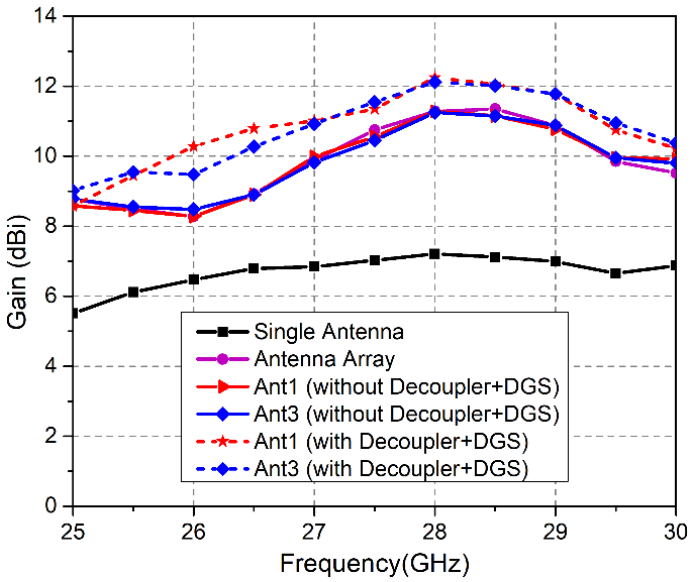

Figure 8. Simulated gain values of the antenna at different design stages.

3. Results and Discussion

In order to validate the characteristics of the proposed antenna, a prototype was fabricated, as shown in Figure 9, and measured experimentally. The fabrication process was carried out using standard PCB technologies. Finally, an investigation on measured and simulated results was performed considering various performance metrics such as reflection coefficient, transmission coefficient, broadside gain, and radiation patterns, as provided in the subsequent sections.

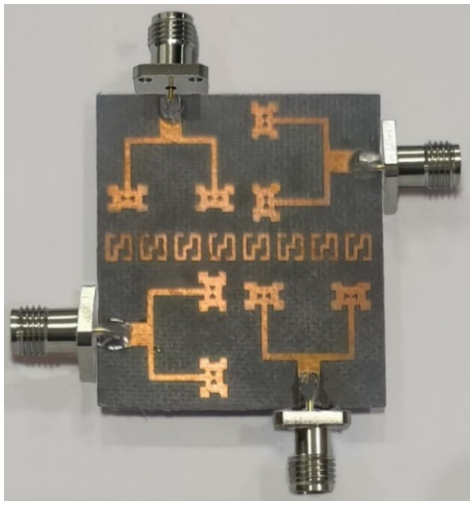

Figure 9. Fabricated antenna prototype.

3.1. Reflection and Transmission Coefficients

Figure 10 illustrates the measured and simulated s-parameter plots for the proposed antennas. The measured reflection coefficient curves ($|S_{11}|$, $|S_{22}|$, $|S_{33}|$, $|S_{44}|$,) are demonstrated in Figure 10a. It can be observed that a resonant band ranging from 27.5 to 28.5 GHz with a −10 dB impedance bandwidth was obtained for the proposed MIMO antennas. Furthermore, the measured transmission coefficient curves $|S_{12}|$, $|S_{13}|$, and $|S_{23}|$ shown in Figure 10b exhibit the isolation of Ant1 from Ant2 and Ant3 as well as the isolation between Ant2 and Ant3. The obtained results show that Ant1 and Ant2 obtained a minimum measured isolation of nearly 40 dB, whereas other antennas resulted in higher isolation values. A comparative analysis of the simulated and measured results demonstrated slight dissimilarities, primarily due to fabrication errors and tolerances of measurement equipment.

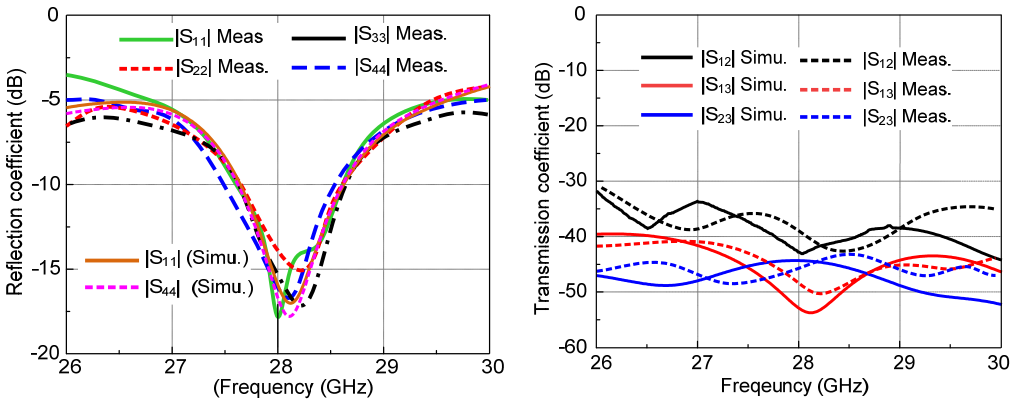

(**a**) (**b**)

Figure 10. Measured and simulated s-parameter plots. (**a**) Reflection coefficient; (**b**) Transmission coefficient of the proposed MIMO antenna.

3.2. Far-Field Results

The far-field measurements were acquired from the anechoic chamber located at the Electromagnetic Wave Technology Institute in Seoul, Korea. The antenna used as a transmitter was a standard horn antenna of the SGH series, whereas the antenna under test was measured as the receiver. The antenna under test was rotated at different orientations to find the measurements at the principal planes of the *E*-plane and the *H*-plane. The radiation patterns (co-polarization and cross-polarization) for Ant1 and Ant2, as shown in Figure 11, were obtained at 28 GHz. It can be noted that maximum radiation occurs

in the boresight direction for Ant1, while for Ant2, a slight tilt in the radiation beam was scanned. Thus, the overall proposed antenna exhibits stable radiation patterns. Likewise, the cross-polarization levels are less than -10dB for all frequencies. The simulated 3D radiation patterns obtained at 28 GHz for Ant1 and Ant2, shown in Figure 12, also depict a similar behavior, as demonstrated by 2D radiation patterns with boresight and tilted radiation, respectively. The peak gain values of 12.2 dBi and 11.7 dBi obtained by both antennas are also illustrated in Figure 12. The simulated and measured gain values attained by the final proposed antenna at various frequencies are also summarized in Table 2. It can be observed that gain varies from 10 to 12 dBi over the entire operational band. The measured gain values in the boresight direction for Ant1 and Ant2 at 28 GHz are 12.02 and 11.46 dBi, respectively. Hence, the simulated and measured results are in substantial agreement with each other.

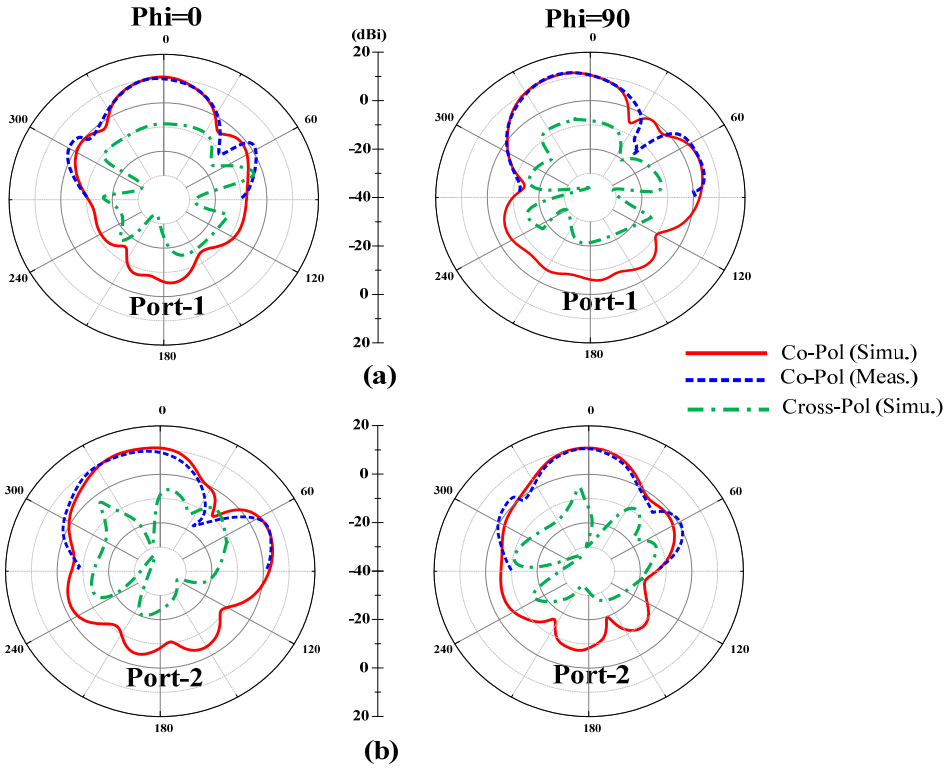

Figure 11. Radiation Patterns at 28 GHz. (**a**) Ant1; (**b**) Ant2.

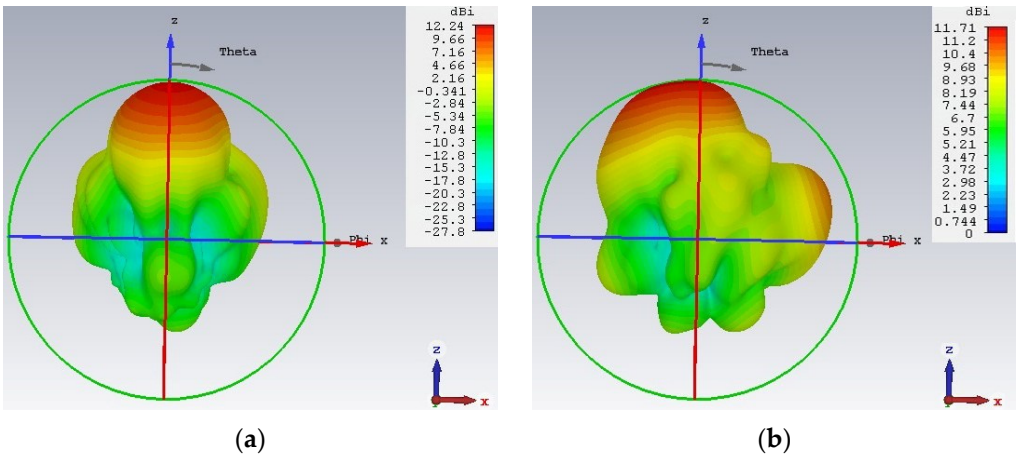

Figure 12. 3D Radiation Patterns at 28 GHz. (**a**) Ant1; (**b**) Ant2.

Table 2. Simulated and measured gain of the MIMO antenna elements.

Freq (GHz)	Ant #	Peak Gain (dBi)	
		Simulated	Measured
27.5	Ant1	10.73	10.25
	Ant2	10.51	10.01
28	Ant1	12.24	12.02
	Ant2	11.71	11.46
28.5	Ant1	11.35	11.12
	Ant2	11.04	10.88

Figure 13 illustrates the radiation efficiency of the proposed MIMO antennas. It can be observed that Ant1 achieved a simulated radiation efficiency of nearly 85%, Ant2 obtained an efficiency of almost 88%, and Ant3 reached approximately 85%. Meanwhile, Ant4 demonstrated a radiation efficiency of nearly 86% over the operational band. The measured radiation efficiencies obtained by Ant1 and Ant2 were 82% and 80%, respectively.

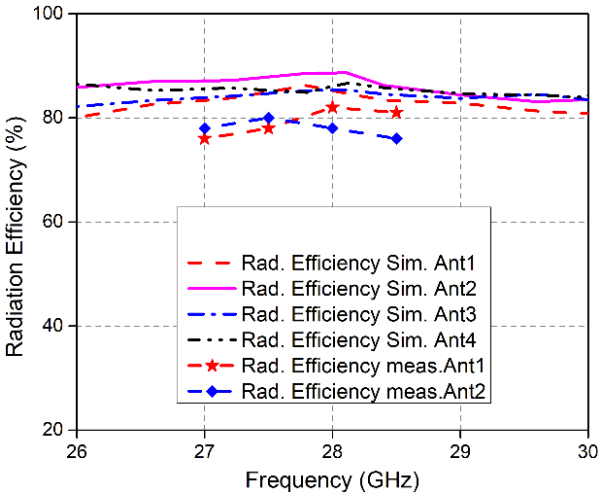

Figure 13. Radiation Efficiency of the proposed MIMO antennas.

3.3. Diversity Performance Analysis

In this section, the diversity performance of the proposed MIMO antenna is explored through different performance metrics such as the Envelope Correlation Coefficient (ECC), Diversity Gain (DG), and Channel Capacity Loss (CCL).

ECC is a substantial parameter for MIMO systems that determines the independence of antenna elements in terms of their individual characteristics [28]. In order to numerically calculate ECC ($\rho_{e,ij}$), the following expression is used [29]:

$$\rho_{e,ij} = \frac{\left|S_{ii} * S_{ij} + S_{ji} * S_{jj}\right|^2}{\left(1 - \left|S_{ii}\right|^2 - S_{ij}{}^2\right)\left(1 - \left|S_{ji}\right|^2 - S_{jj}{}^2\right)} \quad (1)$$

where S_{ii} and S_{ij} are respectively the reflection and transmission coefficients for antenna i and i, j. The ECC curves for the proposed MIMO elements in Figure 14a illustrates that the peak values obtained over the operating band are much smaller than the standard value, thus demonstrating excellent diversity performance.

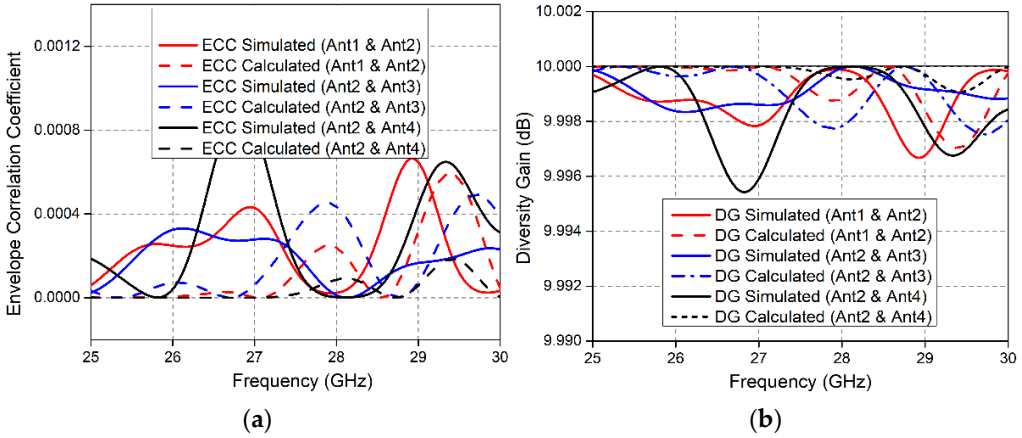

Figure 14. (**a**) ECC and (**b**) DG of the proposed MIMO antenna.

It is likely that diversity gain is another critical metric for analyzing MIMO performance. It can be obtained using Equation (2), as given in [30]:

$$DG = 10\sqrt{1 - \left|\rho_{e,ij}\right|^2} \tag{2}$$

Figure 14b shows that the antenna elements of the proposed MIMO structure attained a DG of nearly 9.999 dB.

In addition to the ECC and DG, CCL is another essential parameter used to assess the MIMO characteristics of an antenna. The capacity loss of the channel due to the correlation between MIMO links is determined by the CCL. It is obtained through the equations provided below [26].

$$C_{(Loss)} = -log_2 det(a) \tag{3}$$

where a is the following correlation matrix:

$$a = \begin{bmatrix} \sigma_{11} & \sigma_{12} \\ \sigma_{21} & \sigma_{22} \end{bmatrix} \tag{4}$$

where

$$\sigma_{ii} = 1 - \left(\left|S_{ii}\right|^2 - \left|S_{jj}\right|^2\right) \tag{5}$$

$$\sigma_{ij} = -\left(S_{ii} * S_{ij} + S_{ji}{S_{jj}}^*\right) \tag{6}$$

Here, σ_{ii} and σ_{ij} denote the correlation coefficients between the antenna elements of a MIMO system. The CCL curves for the proposed MIMO structure shown in Figure 15 demonstrate the high throughput of the system as CCL is below 0.4 bits/s/Hz for the resonating band, which is the standard value and is also accepted in practice.

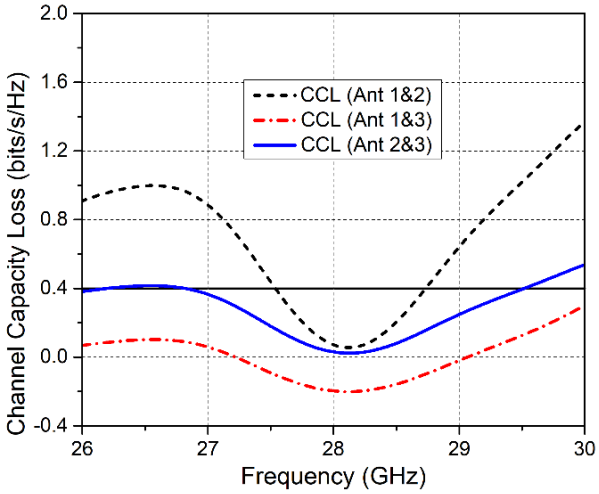

Figure 15. CCL of the proposed MIMO antennas.

4. Comparison with State-of-the-Art Works

Table 3 provides a comparison of the proposed work with other related works recently reported in the literature. It can be observed that most of the MIMO antenna designs reported in [20–26] are large in size as compared to the proposed antenna, which limits their applicability to modern-day compact communication devices. However, few designs which have been able to obtain a compact structure have low gain. Moreover, the isolation obtained for these MIMO structures is low as compared to the proposed MIMO antenna. It is also worth noting that most of the other works have only investigated ECC and DG for MIMO performance; however, this work has also explored CCL for the MIMO system. Therefore, the antenna design proposed in this work, which has a relatively compact size (even the substrate has a low dielectric constant of 2.2), high gain, MIMO capability, and good diversity performance, outperforms other designs and ascertains its suitability for current and impending communication systems.

Table 3. Performance comparison with related works.

Ref	Freq (GHz)	Bandwidth (GHz)	Substrate	Board Size (mm^2)	Number of Ports	Gain (dBi)	Isolation (dB)	ECC, DG (dB)	CCL
[20]	28/38	22.5–29, 33.5–50	Rogers RO 4003C (ε_r = 3.38)	53 × 3.17	2 ports	11.5	20	0.12, >9.4	NP *
[21]	28	24–29, 30.5–36	Rogers RO 4003C (ε_r = 3.38)	126 × 126	81 ports	7.8	20	<0.005, 9.99	NP *
[22]	27/39	25–28.2, 36–41	Rogers RO 4003C (ε_r = 3.38)	26 × 11	2 ports	5, 5.7	>30	0.0001, >9.99	NP *
[23]	28	24–29.9	Rogers RT 5880 (ε_r = 2.2)	52 × 23	2 ports	12.4	>24	<0.0013, >9.9	<0.42
[24]	28/38	23–40	Rogers RT 5880 (ε_r = 2.2)	80 × 80	4 ports	12	>20	<0.0014	NP *
[25]	28	27–28.5	Rogers RT 5880 (ε_r = 2.2)	30 × 30	4 ports	6.1	>29	<0.16, NP	NP *
[26]	28	25.5–29.6	Rogers RO 4350B (ε_r = 3.48)	30 × 35	4 ports	8.3	17	<0.01, >9.96	<0.4
This Work	28	27.5–28.5	Rogers RT 5880 (ε_r = 2.2)	30 × 35	4 ports	12	>40	<0.0003, >9.9	<0.4

* NP: Not Provided.

5. Conclusions

The mm-Wave MIMO antenna is proposed and experimentally validated in this work. The proposed design is a low-profile 4-port MIMO structure, where each MIMO antenna is a 2-element array. In order to enhance the antenna performance, a decoupling structure and

DGS are incorporated. Thus, the involvement of these optimization techniques significantly improved isolation between antenna elements by ≈9 dB. In addition to this, a high gain value of 12 dBi was realized by the proposed antenna design. Owing to salient features such as structural simplicity, compactness, high gain, and good diversity performance with MIMO capability, the proposed antenna befits current and future 5G mm-Wave communication applications.

Future research should focus on obtaining the ultra-wideband operational frequency band while entertaining multiple mm-Wave bands allocated for 5G communication. In addition, the beam steering feature could be introduced for wide coverage. Moreover, sub-6 GHz bands can be introduced along with the mm-Wave bands in the shared aperture designs for the coverage of the maximum 5G frequency bands.

Author Contributions: Conceptualization, M.B. and S.I.N.; Data curation, M.B. and S.I.N.; Formal analysis, M.B., S.I.N. and N.H.; Investigation, Y.A. and N.K.; Methodology, M.B. and S.I.N.; Project administration, Y.A.; Resources, N.H. and N.K.; Software, N.K.; Supervision, S.I.N. and Y.A.; Validation, M.B. and S.I.N.; Visualization, N.H. and N.K.; Writing—original draft, M.B.; Writing—review & editing, S.I.N., N.H., Y.A. and N.K. All authors have read and agreed to the published version of the manuscript.

Funding: This work was supported by Institute for Information & communications Technology Promotion (IITP) grant funded by the Korea government (MSIP) (No. 2021-0-00490, Development of precision analysis and imaging technology for biological radio waves).

Conflicts of Interest: The authors declare no conflict of interest.

References

1. Vannithamby, R.; Talwar, S. (Eds.) *Towards 5G: Applications, Requirements and Candidate Technologies*; John Wiley & Sons: Hoboken, NJ, USA, 2017; ISBN 978-1-118-97991-4. Available online: https://www.wiley.com/en-us/Towards+5G%3A+Applications%2C+Requirements+and+Candidate+Technologies-p-9781118979914 (accessed on 30 September 2021).
2. da Silva, M.M.; Guerreiro, J. On the 5G and Beyond. *Appl. Sci.* **2020**, *10*, 7091. [CrossRef]
3. Hilt, A. Availability and Fade Margin Calculations for 5G Microwave and Millimeter-Wave Anyhaul Links. *Appl. Sci.* **2019**, *9*, 5240. [CrossRef]
4. Varga, P.; Peto, J.; Franko, A.; Balla, D.; Haja, D.; Janky, F.; Soos, G.; Ficzere, D.; Maliosz, M.; Toka, L. 5G support for Indus-trial IoT Applications—Challenges, Solutions, and Research gaps. *Sensors* **2020**, *20*, 828. [CrossRef] [PubMed]
5. Qualcomm Technologies Inc. Spectrum for 4G and 5G. 2017. Available online: https://www.qualcomm.com/news/media-center (accessed on 30 September 2021).
6. European 5G Observatory. National 5G Spectrum Assignment. Available online: https://5gobservatory.eu/ (accessed on 10 May 2020).
7. Shayea, I.; Rahman, T.A.; Azmi, M.H.; Islam, R. Real Measurement Study for Rain Rate and Rain Attenuation Conducted over 26 GHz Microwave 5G Link System in Malaysia. *IEEE Access* **2018**, *6*, 19044–19064. [CrossRef]
8. Hussain, N.; Jeong, M.J.; Park, J.; Kim, N. A broadband circularly polarized Fabry-Perot resonant antenna using a sin-gle-layered PRS for 5G MIMO applications. *IEEE Access* **2019**, *7*, 42897–42907. [CrossRef]
9. Nguyen-Trong, N.; Tran, H.H.; Nguyen, T.K.; Abbosh, A.M. A Compact Wideband Circular Polarized Fabry-Perot Antenna Using Resonance Structure of Thin Dielectric Slabs. *IEEE Access* **2018**, *6*, 56333–56339. [CrossRef]
10. Lin, Q.W.; Wong, H.; Zhang, X.Y.; Lai, H.W. Printed Meandering Probe-Fed Circularly Polarized Patch Antenna with Wide Bandwidth. *IEEE Antennas Wirel. Propag. Lett.* **2014**, *13*, 654–657. [CrossRef]
11. Wong, H.; Lin, Q.W.; Lai, H.W.; Zhang, X.Y. Substrate integrated meandering probe-fed patch antennas for wideband wire-less devices. *IEEE Trans. Compon. Packag. Manuf. Technol.* **2015**, *5*, 381–388. [CrossRef]
12. Hussain, N.; Nguyen, T.K.; Han, H.; Park, I. Minimum Lens Size Supporting the Leaky-Wave Nature of Slit Dipole Antenna at Terahertz Frequency. *Int. J. Antennas Propag.* **2016**, *2016*, 1–8. [CrossRef]
13. Song, Z.; Zheng, H.; Wang, M.; Li, E.; Li, Y. Design of One-Eighth Spherical Dielectric Resonator Antenna for 5G Applications. *IEEE Access* **2020**, *8*, 9480–9487. [CrossRef]
14. Dzagbletey, P.A.; Jung, Y.-B. Stacked Microstrip Linear Array for Millimeter-Wave 5G Baseband Communication. *IEEE Antennas Wirel. Propag. Lett.* **2018**, *17*, 780–783. [CrossRef]
15. Khalily, M.; Tafazolli, R.; Xiao, P.; Kishk, A.A. Broadband mm-Wave Microstrip Array Antenna with Improved Radiation Characteristics for Different 5G Applications. *IEEE Trans. Antennas Propag.* **2018**, *66*, 4641–4647. [CrossRef]
16. Naqvi, S.I.; Naqvi, A.H.; Arshad, F.; Riaz, M.A.; Azam, M.A.; Khan, M.S.; Amin, Y.; Loo, J.; Tenhunen, H. An Integrated Antenna System for 4G and Millimeter-Wave 5G Future Handheld Devices. *IEEE Access* **2019**, *7*, 116555–116566. [CrossRef]

17. Araújo, D.C.; Maksymyuk, T.; De Almeida, A.L.F.; Maciel, T.F.; Mota, J.C.; Jo, M. Massive MIMO: Survey and future re-search topics. *IET Commun.* **2016**, *10*, 1938–1946. [CrossRef]
18. Sethi, W.T.; Ashraf, M.A.; Ragheb, A.; Alasaad, A.; Alshebeili, S.A. Demonstration of Millimeter Wave 5G Setup Employing High-Gain Vivaldi Array. *Int. J. Antennas Propag.* **2018**, *2018*, 1–12. [CrossRef]
19. Jeong, M.J.; Hussain, N.; Park, J.W.; Park, S.G.; Rhee, S.Y.; Kim, N. Millimeter-wave microstrip patch antenna using vertical-ly coupled split ring metaplate for gain enhancement. *Microw. Opt. Technol. Lett.* **2019**, *61*, 2360–2365. [CrossRef]
20. Saad, A.A.R.; Mohamed, H.A. Printed millimeter-wave MIMO-based slot antenna arrays for 5G networks. *AEU Int. J. Electron. Commun.* **2019**, *99*, 59–69. [CrossRef]
21. Wang, F.; Duan, Z.; Wang, X.; Zhou, Q.; Gong, Y. High Isolation Millimeter-Wave Wideband MIMO Antenna for 5G Communication. *Int. J. Antennas Propag.* **2019**, *2019*, 4283010. [CrossRef]
22. Ali, W.; Das, S.; Medkour, H.; Lakrit, S. Planar dual-band 27/39 GHz millimeter-wave MIMO antenna for 5G applications. *Microsyst. Technol.* **2020**, *27*, 283–292. [CrossRef]
23. Al-Bawri, S.S.; Islam, M.T.; Shabbir, T.; Muhammad, G.; Islam, S.; Wong, H.Y. Hexagonal Shaped Near Zero Index (NZI) Metamaterial Based MIMO Antenna for Millimeter-Wave Application. *IEEE Access* **2020**, *8*, 181003–181013. [CrossRef]
24. Sehrai, D.A.; Abdullah, M.; Altaf, A.; Kiani, S.H.; Muhammad, F.; Tufail, M.; Irfan, M.; Glowacz, A.; Rahman, S. A Novel High Gain Wideband MIMO Antenna for 5G Millimeter Wave Applications. *Electronics* **2020**, *9*, 1031. [CrossRef]
25. Kamal, M.; Yang, S.; Ren, X.-C.; Altaf, A.; Kiani, S.; Anjum, M.; Iqbal, A.; Asif, M.; Saeed, S. Infinity Shell Shaped MIMO Antenna Array for mm-Wave 5G Applications. *Electronics* **2021**, *10*, 165. [CrossRef]
26. Khalid, M.; Naqvi, S.I.; Hussain, N.; Rahman, M.; Fawad; Mirjavadi, S.S.; Khan, M.J.; Amin, Y. 4-Port MIMO Antenna with Defected Ground Structure for 5G Millimeter Wave Applications. *Electronics* **2020**, *9*, 71. [CrossRef]
27. Balanis, C.A. *Antenna Theory: Analysis and Design*, 3rd ed.; Wiley Interscience: Hoboken, NJ, USA, 2005; ISBN 047166782X.
28. Blanch, S.; Romeu, J.; Corbella, I. Exact representation of antenna system diversity performance from input parameter description. *Electron. Lett.* **2003**, *39*, 705. [CrossRef]
29. Sharawi, M.S. Printed Multi-Band MIMO Antenna Systems and Their Performance Metrics [Wireless Corner]. *IEEE Antennas Propag. Mag.* **2013**, *55*, 218–232. [CrossRef]
30. Sharawi, M.S. *Printed MIMO Antenna Engineering*; Artech House: Norwood, MA, USA, 2014; ISBN 9781608076819.